Deep-Subwavelength Direction-Of-Arrival Detection with Enhanced Sensitivity Using Temporal Modulation

Tamir Zchut and Yarden Mazor [*]

School Of Electrical Engineering, Tel Aviv University, Tel Aviv 69978, Israel

Electromagnetic wave interaction with time-varying systems has gained a lot of research interest in recent years. The temporal modulation gives unprecedented control over the response, allowing us to go beyond the state of the art in passive systems. In this work, we use time variation and show it can enhance the direction-of-arrival sensitivity of a deeply subwavelength dimer, using the added to degrees of freedom. We formulate the problem, derive an analytical model, and discuss the various physical mechanisms responsible for the enhancement. We show that time modulation enables an alternative degree of control that can be used to optimize the response for various incident frequencies, allowing for wideband operation. Additionally, we show that incorporating the currents from higher generated harmonics into the sensing scheme allows us to extract more accurate information about the impinging wave.

I. INTRODUCTION

Detecting a wave's direction of arrival (DOA) has useful applications in many fields. Starting from the survival of small species in nature, which rely on understanding the direction a predator is approaching based on the sounds it makes, through aviation and radar systems, and even modern-day imaging technologies such as light-field photography. Usually, DOA detectors rely on the phase differences when the EM signal is recorded by two (or more) adjacent elements, bringing forward a significant limitation—what if the difference is very small, as when the sensing apparatus is small compared to the received signal's characteristic wavelength?

Two main approaches exist in electromagnetic (EM) waves to alleviate this limitation. One approach is based on biomimicking small insects. In large animals, significant ear separation lets information regarding the DOA be extracted from the phase and amplitude difference of the recorded sound. In small insects, this problem is mitigated by direct coupling between the ears. This approach is simple to implement and works very well, mainly around a prescribed angle [1]. This was followed up by further optimization, including using high-order modes [2] and non-Foster coupling networks [3]. The second approach is using multiphysics systems. One can couple the EM wave response to a different wave mechanism that operates in similar frequencies but significantly smaller wavelengths, which enhances the recorded signal difference. This is demonstrated for an electroacoustic system in Ref. [4].

On a parallel route, in the past decade, EM wave interaction with time-varying systems has seen a burst of renewed interest, driven by two parallel processes. First, the ability to implement such systems has seen significant advances, making the theoretical ideas more realistic. Second, the rise of metamaterials has pointed to many intriguing and exotic wave phenomena occurring in materials with extreme parameters. The basic theoretical concepts are introduced in Refs. [5,6], and numerous applications have been proposed, and among the ones that are more relevant to this work we have the implementation of nonreciprocal elements (gyrators [7], circulators, and isolators [8,9]), Nonreciprocal transmission-line design [10], extreme energy accumulation [11], nonreciprocal reflection and transmission [12,13], and improved antenna matching, and bandwidth [14–17] (many other applications are summarized in [18,19]). Of specific relevance are the control of Mie-scattering properties, shown in Ref. [20]. Nonperiodic variation and switching also play a key role, demonstrated for broadband matching [21], matched filter design [22], engineered time-reversal spectrum [23], and many more.

In this work, we examine how we can enhance the sensitivity of DOA detection in deeply subwavelength systems using a different approach—by incorporating temporal modulation to enhance and tailor the physical interactions between the system elements. Time variation adds several degrees of freedom to our system, which can be used to improve performance. Frequency conversion processes can couple the signal to predesigned resonances, which increase conversion efficiency and sensitivity. Phase-dependant parametric gain may increase the

*yardenm2@tauex.tau.ac.il

amplitude of measured currents and differential DOA response of the system components. Since time-modulated systems naturally have many parameters at play, and rich content of physical processes occurring, we focus on unveiling the physical mechanisms at play that enable sensitivity enhancement.

Several works have already started examining this avenue of time-modulated DOA systems. First, in Ref. [24] and subsequent works, periodic switching of the received signal from a DOA sensing dimer is used to enable angle estimation through the ratio of power content in various higher harmonics. However, since only the received signal is switched, physical interaction between the elements does not benefit from these higher harmonics. Moreover, the coupling between the elements, which is pivotal in this work, does not play a significant role. This makes this strategy viable mostly for $d > \lambda/2$, and not the deeply subwavelength scenario we target. In Ref. [25], a time-modulated metasurface is proposed for DOA detection, leveraging the deviations in the diffraction and reflection angles to do the estimation. Again, this work utilizes a system whose size is on the order of λ.

II. FORMULATION

Naturally, time-modulated wave systems possess many degrees of freedom. On top of the "regular" time-invariant parameters, we also have the modulation frequency, depth, waveform, and the ensuing coupling to higher and lower frequencies. Due to that, the analysis becomes complicated quite rapidly with the addition of components. Since we aim to focus on the physical mechanisms that enhance the DOA sensitivity, we employ a simple model—a two-dimensional (2D) dimer. To explore our concept, we use a dimer composed of two infinite wires made of a perfect electric conductor (PEC), as shown in Fig. 1. The incident wave angle θ corresponds to a phase difference of $kd\cos(\theta) \ll 1$. The wires are periodically loaded with $Z_L = Z_S + Z_C$, where Z_S is a static, nonmodulated impedance, and Z_C is the imepdance representing the time-modulated capacitor $C(t)$. The wires are modeled using their susceptibility α, which determines the induced current $I(\omega)$ (without modulation) on each wire via

$$I(\omega) = \alpha(\omega)E_{\tan}^{\text{loc}}(\omega), \quad (1)$$

Where $E_{\tan}^{\text{loc}}(\omega)$ is the tangential component of the local field, which contains both the incident wave, and the field scattered by the other wire, but in the absence of the examined wire itself. For infinite PEC wires, the susceptibility is [26,27]

$$\alpha^{-1}(\omega) = \alpha_0^{-1}(\omega) + \frac{Z_L}{\Delta}, \quad \alpha_0^{-1}(\omega) = \frac{\eta k}{4}H_0^{(2)}(kr_0), \quad (2)$$
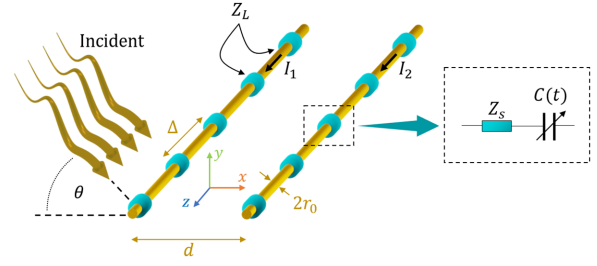

FIG. 1. Dimer model: two infinite wires, with periodic loading $Z_L = Z_S + Z_C$, where Z_S is a static impedance, and Z_C is the impedance of a time-modulated capacitor.

where α_0 is the susceptibility of the unloaded wires, Z_L is the Δ-periodic loading, η is the medium impedance, k is the free-space wave number, and $H_0^{(2)}$ is zero-order Hankel function of the second kind. To clarify the notation, later we use also $\gamma = \alpha^{-1}, \gamma_0 = \alpha_0^{-1}$, and for simplicity, we focus on TE incidence (therefore, $\hat{z}$ electric field). For every frequency ω, the current on the wires generates scattered fields via $E_{\tan}^{\text{scattered}}(\rho) = G(\rho, \omega)I$, where $G(\rho, \omega)$ is the 2D Green's function of the electric field in free space, i.e., $G(\rho, \omega) = -(\eta k(\omega)/4)H_0^{(2)}(k(\omega)\rho)$.

Using both G and α, we can express the total reaction of a nonmodulated dimer are

$$I_2 = \frac{\alpha_2 E_2^{\text{inc}} + G(d)\alpha_1\alpha_2 E_1^{\text{inc}}}{1 - G^2(d)\alpha_1\alpha_2}, \quad I_1 = \alpha_1\left(E_1^{\text{inc}} + G(d)I_2\right). \quad (3)$$

Now, let us incorporate the effects of periodic temporal modulation into the system. When the capacitor $C(t)$ is periodically modulated, $C(t)^{-1} = C_0^{-1}[1 + m\cos(\omega_m t + \varphi_m)]$, we can represent every physical quantity as a sum of all the possible harmonics

$$X(t) = \sum_{n=-\infty}^{\infty} \tilde{X}_n e^{j(\omega+n\omega_m)t} + \text{c.c.} = \sum_{n=-\infty}^{\infty} \tilde{X}_n e^{j\omega_n t} + \text{c.c.}, \quad (4)$$

where X can be the current I or the electrical field E or any other relevant quantity, $\omega_n = \omega + n\omega_m$, and c.c. means complex conjugate. Since both the current I and the electric field E_z are excited in multiple frequencies (as expected in our temporally modulated system), the amplitudes of the spectral components can be ordered in a column vector $[\tilde{I}]$, and $[\tilde{E}]$. Using these, and following Refs. [6,26], we can write the time-modulated single wire response:

$$[\tilde{E}] = \underline{\underline{\Gamma}}[\tilde{I}] \leftrightarrow \begin{bmatrix} \vdots \\ \tilde{E}_{-1} \\ \tilde{E}_0 \\ \tilde{E}_1 \\ \vdots \end{bmatrix} = \begin{bmatrix} \ddots & \vdots & \vdots & \vdots & 0 \\ \cdots & \gamma_0(\omega_{-1}) + \frac{1}{j\omega_{-1}C_0\Delta} & \frac{M}{j\omega_0 C_0\Delta} & 0 & \cdots \\ \cdots & \frac{M^*}{j\omega_{-1}C_0\Delta} & \gamma_0(\omega_0) + \frac{1}{j\omega_0 C_0\Delta} & \frac{M}{j\omega_1 C_0\Delta} & \cdots \\ \cdots & 0 & \frac{M^*}{j\omega_0 C_0\Delta} & \gamma_0(\omega_1) + \frac{1}{j\omega_1 C_0\Delta} & \cdots \\ 0 & \vdots & \vdots & \vdots & \ddots \end{bmatrix} \begin{bmatrix} \vdots \\ \tilde{I}_{-1} \\ \tilde{I}_0 \\ \tilde{I}_1 \\ \vdots \end{bmatrix}, \quad (5)$$

where $M = me^{j\varphi_m}$. Since the current is excited in several frequencies, each of these will generate a scattered field at its specific frequency. Since G is a function of the frequency ω, it can be formulated using a diagonal matrix, $\underline{\underline{G}}$

$$\underline{\underline{G}}(\rho) = \text{diag}[\cdots, G(\rho, \omega_{-1}), G(\rho, \omega_0), G(\rho, \omega_1), \ldots]. \quad (6)$$

Then, for the modulated dimer, the currents can be solved from the following matrix equation:

$$\underline{\underline{\Gamma}}_1[\tilde{I}_1] - \underline{\underline{G}}[\tilde{I}_2] = [\tilde{E}_1^i], \quad \underline{\underline{\Gamma}}_2[\tilde{I}_2] - \underline{\underline{G}}[\tilde{I}_1] = [\tilde{E}_2^i]. \quad (7)$$

A. Performance metrics and operation

In order to compare the performance and possible benefits of our approach, both with respect to different modulation scenarios and other enhancement schemes, we use the sensitivity S, defined as

$$S(\theta) = \left| 1 - \frac{I_1(\theta)}{I_2(\theta)} \right|^2, \quad (8)$$

which essentially quantifies the relative variation of I_1, I_2 with respect to the incident angle. To accurately extract θ from I_1, I_2, S should vary with large amplitude against θ.

In addition to the sensitivity, we would also like to define a more simple metric, that will allow us to capture the properties of $S(\theta)$ using a single scalar. This will allow us to characterize the sensitivity curve against various system parameters (wire loading, temporal modulation parameters). To that end, we use the maximum sensitivity, $S_{\max}$:

$$S_{\max} = \max_\theta \{S(\theta)\}. \quad (9)$$

In the modulated system, $S_{\max}$ can be calculated for the different up- and down-converted harmonics (which will prove very beneficial), and therefore we often use $S_{\max}^n$ to indicate that it is calculated for the n'th harmonic, where $n = 0$ is the fundamental, incident frequency. $S_{\max}^{NM}$ (or any other occurrence of NM) indicates the nonmodulated case.

The currents in the wires I_1, I_2 would constitute the measured quantities in a practical scenario. Using Eq. (8), the sensitivity S can be calculated, and matched against a theoretical $S(\theta)$ graph, which is depicted later, in Sec. III C, to extract the DOA. Additional signal processing can be used to enhance the acquired signal but is not necessary in order to calculate the DOA.

III. RESULTS AND DISCUSSION

A. Frequency-conversion effects

Various physical mechanisms play a role in enhancing the sensitivity of the dimer response to the DOA. To discuss these systematically, let us start by looking at the $S_{\max}^n / S_{\max}^{NM}$ versus the modulation frequency. Figure 2 shows $S_{\max}^{\{-1,0,1\}}$ for the following parameters: the radius of the wire is $r_0 = 0.3$ mm, the distance between the wires is $d = 5$ cm, and the base frequency is $f_0 = 300$ MHz. The period of loading is $\Delta = 1$ cm, with the load consisting of a periodic resistor $R_L = 0.3$ mΩ, and a capacitance $C^{-1}(t) = C_0^{-1}(1 + m\cos(\omega_m t))$, where $C_0 = 13$ pF and $m = 0.2$. In this work we examine the case where all load capacitors are modulated in the same manner. However, our formulation can be adapted to work with more complex modulation schemes, where either the capacitors loading a certain wire are modulated with some waveform, or there is a variance between the wires.

In the fundamental frequency, we see that mostly $S^{\max}$ is similar to the nonmodulated case (yielding a normalized value close to 1), except for a small region around $\omega_m \approx 2.4\omega$ which exhibits a moderate improvement, $S_{\max}^0 / S_{\max}^{NM} \approx 2.7$. However, when looking at the higher harmonics, we see that the sensitivity becomes much higher at certain values of ω_m ($\omega_m \approx 0.21\omega, 0.42\omega, 2.4\omega$). The effect behind this is composed of the interaction of two mechanisms: the eigenmodes of the dimer and frequency conversion induced by the temporal modulation. In the unmodulated dimer, each wire, incorporated with capacitive loading, is resonant (since the pristine wire response is inductive). When two such resonant wires are placed next to each other to form a dimer, two resonance frequencies exist. Each resonant frequency is characteristic of a specific dimer mode—a symmetric and an anti-symmetric one that form a basis for any current combination that may
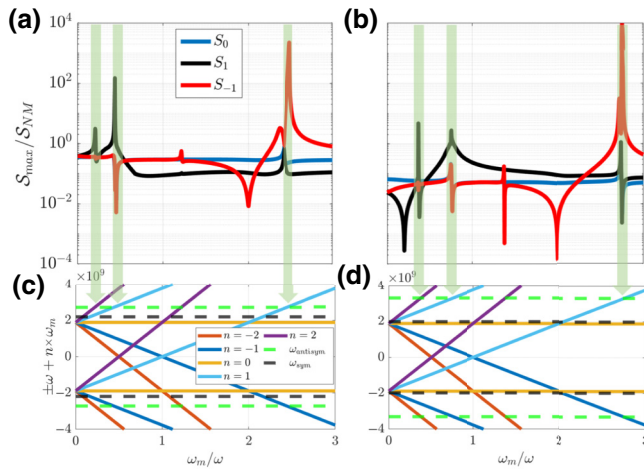
FIG. 2. (a) Maximum sensitivity as a function of ω_m/ω for harmonies $-1, 0, 1$, and $d = 5$ cm (b) the same, for $d = 1$ cm (c) frequency-conversion map for $\pm\omega + n\omega_m$, with $-2 \leq n \leq 2$, and the symmetric and antisymmetric resonance frequencies. The green arrows indicate connection between peaks in the sensitivity and intersection in the resonance map. (d) Same, for $d = 1$ cm.

be excited in the wires. We denote the resonance frequencies of each of these modes $\omega_{\text{sym}}, \omega_{\text{antisym}}$, respectively. How strongly each dimer mode contributes to the total currents is a function of the excitation frequency and the exciting field distribution. Since we want to extract information regarding the DOA from the differences between the currents, we would like to "boost" the content of the antisymmetric mode as much as possible and how steeply this content varies as a function of the incidence angle (considering that for certain values of θ, namely $\pi/2$ and $3\pi/2$, there is only the symmetric mode, regardless of other parameters, due to symmetry considerations).

When considering a deep subwavelength dimer, we expect the content of the symmetric mode to be dominant, resulting from the slight difference in exciting field between the dimer wires. This makes the current differences between the wires vary only slightly when changing θ, making it harder to extract information about the DOA.

When adding periodic temporal modulation, another mechanism behind the sensitivity enhancement comes into play—frequency conversion. When the capacitor is allowed to vary with time, we convert the fields in the basic problem to higher (and possibly lower) frequencies, i.e., $\omega_n = \omega_0 + n\omega_m$. When ω_m is chosen such that one of the ω_n frequencies coincides with ω_{antisym} we can obtain a strongly enhanced antisymmetric mode content in the corresponding n'th harmonic, which is also steeply dependant on the incident angle θ. This results in an enhanced S_{max}^n for that corresponding harmonic, as seen in Figs. 2(a) and 2(b) for dimer separation $d = 5$ cm, 1 cm, respectively.

Using Figs. 2(c) and 2(d), we can see the correlation between these two mechanisms, which enhance the

sensitivity. The continuous lines represent different ω_ns as a function of ω_m, and the dashed lines show the resonance frequency of the symmetric and antisymmetric modes in the unmodulated dimer. When a continuous line intersects the green dashed line, $\omega_n = \omega_{\text{antisym}}$ is satisfied for that n'th harmonic, the ω_m values that yield this intersection are roughly the modulation frequencies where we experience a sharp increase in the sensitivity. Thus, by choosing the dimer parameters, we can alter ω_{antisym} and ω_m, and tailor the frequency response we need, to sense the expected θs better for the required range of operating frequencies. It is essential to add here that while this proves good physical intuition, quantitatively, there are minor deviations in the predicted value of ω_m based on this intuition and the actual value in which the enhancement is most prominent. This is due to the fact that we make use of the resonance frequencies in the *unmodulated system*. These frequencies also experience a shift under modulation since the effective wire impedances are altered.

Next, we would like to explore additional venues to tune the performance of our dimer. The natural way to do that, is by tailoring the periodic loading Z_L using additional passive elements such as inductors, capacitors, or a combination of the two.

To simplify the calculation we add the components in series. When adding either an inductance L or capacitance C, the load impedance Z_L in the n'th harmonic becomes $Z_L(\omega_n) = R_l + (1/j\omega_n C_m) + j\omega_n L$ or $Z_C(\omega_n) = R_l + (1/j\omega_n C_m) + (1/j\omega_n C)$, respectively. Figure 3 presents the sensitivity dynamics as a function of the values of L, C. In (a), (b), (d), (e) we see the sensitivity of both the base harmony S_0 and the first harmony S_1, as a function of the added passive element [L for (a), (d) or C for (b), (e)] and of the normalized modulation frequency ω_m/ω. In all these panels, we see that as the passive element value, L or C, changes, the modulation frequency of the peak ω_m^{peak} changes as well. In these panels, the red line shows the location of the antisymmetric resonance frequency for the nonmodulated circuit, and the yellow lines show the location of the symmetric resonance frequency. As portrayed before, the sensitivity peak modulation frequency moves together with the conversion frequency corresponding to the antisymmetric mode. These panels show that this concept can be generalized, and the loading can be used to tailor the response to our needs.

When combining inductance and capacitance, we introduce more resonance frequencies into the nonmodulated system, which provide additional sensitivity peaks when coinciding with converted harmonics. For example, when using $Z_L(\omega_n) = R_l + \{1/j\omega_n C_m + [1/j\omega_n L + (1/j\omega_n C)]\}$ we see in Figs. 3(c) and 3(f) how additional peaks for different ω_m values are added to the system, which can be used to design a multifrequency sensing dimer. In Fig. 3(g), we see how a change to the modulation capacitor

controls the specific θ around which the sensitivity changes most drastically. For each value of C_0 the optimal ω_m is chosen, and S^1 is calculated.

B. Energy balance and conversion efficiency

Since our system is time modulated it is not, in general, passive. Here, we want to examine the balance between the incident power used to excite the currents P_{inc} and the radiated power P_{rad} to better understand the energy dynamics. Assuming that no material losses are present, the only way energy can exit the system is through radiation. In reality, there are some losses to the wires and the system elements, but the dissipated power is negligible in comparison with the radiated power. If we define a cylindrical envelope $\mathcal{S}$ with radius $R \to \infty$, the radiated power is given by (Appendix)

$$P_{scat}(\omega) = \frac{\eta^2 k}{4}\left(\left[|I_1|^2 + |I_2|^2\right] + 2J_0(kd)\mathrm{Re}\left\{I_1 I_2^*\right\}\right),\tag{10}$$

where $J_0(z)$ is 0th order Bessel function. On the other hand, the power extracted from the incident field, $P_{inc}(\omega)$ is given by

$$P_{inc}(\omega) = \frac{1}{2}\mathrm{Re}\left\{\alpha^*(|\bar{E}_1^{inc}|^2 + \bar{E}_1^{inc}G^*(d)\bar{I}_2^*)\right\}$$
$$+ \frac{1}{2}\mathrm{Re}\left\{\alpha^*(|\bar{E}_2^{inc}|^2 + \bar{E}_2^{inc}G^*(d)\bar{I}_1^*)\right\}.\tag{11}$$

When the system is not modulated and lossless, these quantities will be in equilibrium. When time modulation is introduced, this equilibrium is violated, since the modulation can potentially provide additional power to the system (or act as a sink and extract power). In this case, there are additional frequencies in which current is generated, and therefore power is radiated, rendering the total scattered power as a sum over all possible frequencies $P_{scat,tot} = \sum_n P_{scat}(\omega_n)$. In Fig. 4(a), we examine the total power gain (blue) and the up- and down-converted scattered power as a function of the modulation frequency ω_m. For each choice of ω_m the obtained scattered power is also a function of the incidence angle θ, and since we would like to examine these dynamics, we represent each quantity by two different lines: a thick line, which depicts the minimal power as a function of θ, $\min_\theta\{P_{scat}\}$, and a thin line, which depicts the maximal energy as a function of θ, $\max_\theta\{P_{scat}\}$. Across all examined modulation frequencies a small amount of total gain is provided to the system, since the blue line in Fig. 4(a) is always > 1. Additionally, in certain values of ω_m we see there is a significant difference between the maximum and minimum for different DOA θ. This is a complementary mechanism—when the modulation frequency up- or down-converts to the antisymmetric dimer mode, the gain provided to the system has a significant variation as a function of θ, playing a role in the resulting enhanced sensitivity to the DOA. Figure 4(b) helps us confirm this picture. We see that the total scattered energy in each harmonic experiences a noticeable dependence on θ (manifesting as a gap between the
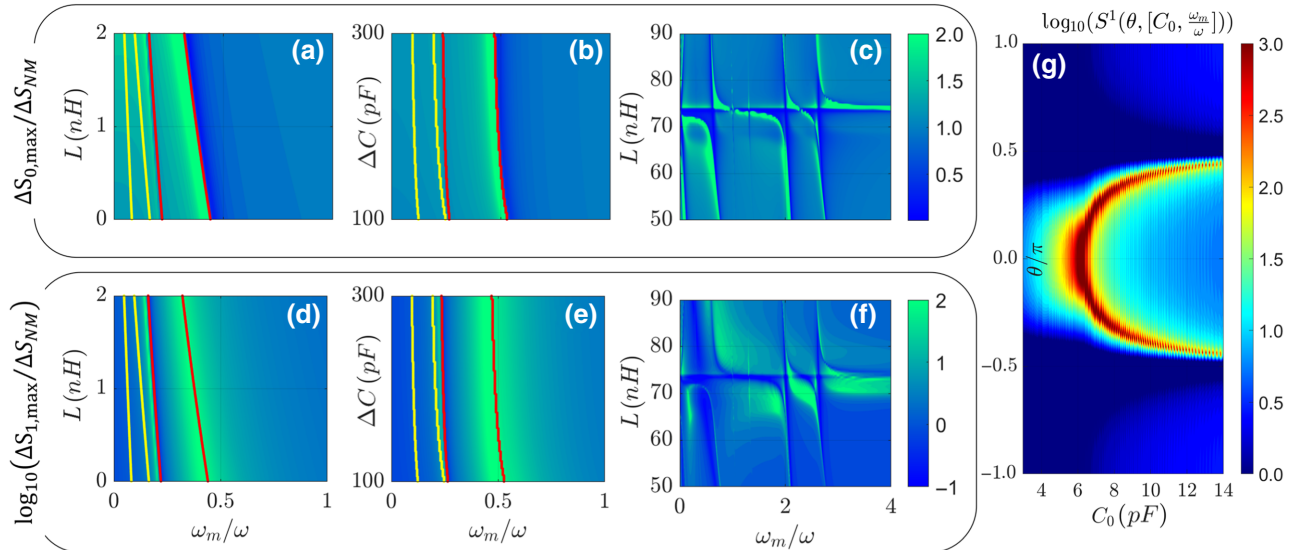

FIG. 3. (a)–(c) Normalized maximum sensitivity in the fundamental harmonic, as a function of ω_m/ω, and of the value of inductance and capacitance added to Z_L. (d)–(f) Normalized sensitivity of the first harmonic, as a function of ω_m/ω, and of the value of inductance and capacitance, on a logarithmic scale. The red lines are the evaluated ω_m required for the first harmonic to coincide with the antisymmetric resonance frequency of the nonmodulated circuit (yellow for the symmetric resonance). For (c),(f), $C = 3pF$; (g), $S^1(\theta)$ for varying values of C_0.
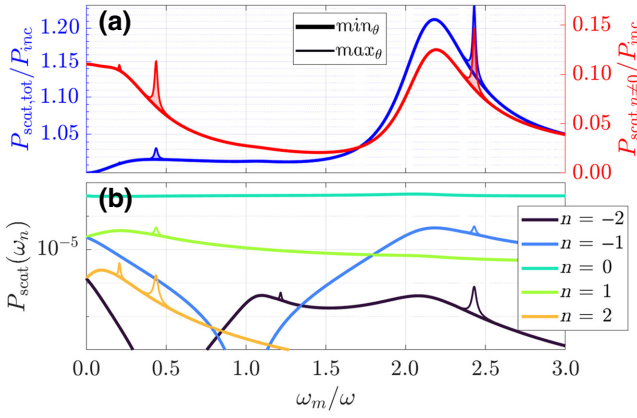
FIG. 4. (a) Normalized sum of the total scattered energy (in all harmonics) (blue), and normalized sum of scattered energy in the up- and down-converted harmonics (excluding the fundamental $n = 0$) of the scattered energy (red). (b) Scattered energy of five harmonies $-2 < n < 2$. Both are functions of the normalized modulation frequency ω_m/ω_0, and show the difference between the minimal energy as a function of θ (thick line), and the maximum energy as a function of θ (thin line).

FIG. 5. (a) Variation of the current in the fundamental, and first up-converted harmonic as a function of θ, for the parameters given in Sec. III A, $\omega_m/\omega = 0.438$. (b) The values of $S^0[\theta]$ (continuous orange) and $S^1[\theta]$ (blue) for $\omega_m/\omega = 0.438$ and in purple for $\omega_m/\omega = 0.432$. For comparison, $S_{NM}[\theta]$ is shown in the dashed line. (c) Same as (b), this time showing $dS/d\theta$.

thick and thin lines) when the conversion corresponds to the antisymmetric dimer mode. When examining the normalized sum of the converted harmonics (all $n \neq 0$) (red), we see that for modulation frequencies corresponding to conversion to dimer resonances the scattered power is 3 times larger, which indicates the much higher conversion efficiency in this regime.

In Fig. 4(a)(red), we notice two types of peaks in sensitivity—peaks for which the amplitude varies as a function of θ (manifesting as a significant gap between maximum and minimum values), and peaks, which do not have this "spreading." Another characteristic that is different between these is the width of the peaks. The peaks associated with the antisymmetric mode are much narrower than the symmetric one. This is due to the fact that the antisymmetric mode has a significantly higher-quality factor (Q factor), a consequence of the fact that the primary "loss" mechanism here is radiation, and the antisymmetric mode radiates much less efficiently. This can be seen using the scattered energy equation, Eq. (10)—for given current magnitude on each wire, when the currents are out of phase ($I_1 = -I_2$) we have $I_1 I_2^* < 0$, while for the symmetric mode $I_1 I_2^* > 0$. Since $J_0(kd) \approx 1$, the expected radiated power will be much higher for the symmetric mode than for the antisymmetric mode.

C. Angular response examples

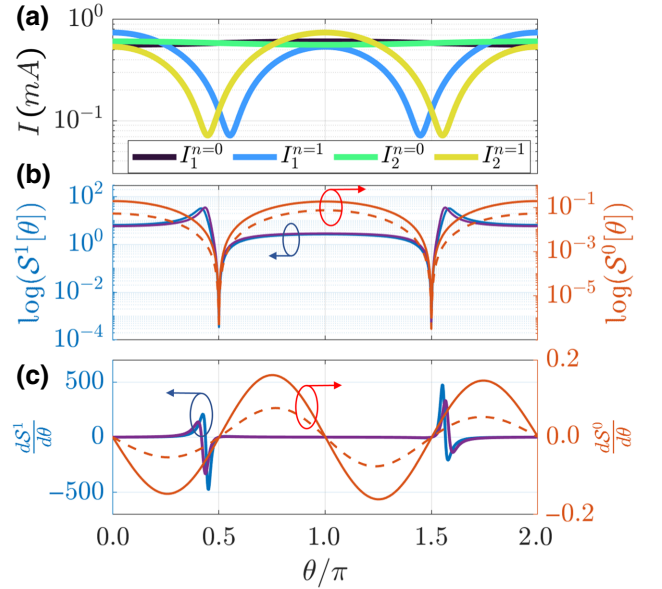To obtain a better grasp of the dimer response, and the variation as a function of the DOA, let us examine it for a specific choice of parameters. Figure 5(a) shows the current in the wires versus θ for $\omega_m/\omega = 0.438$, where we see how the first harmonic currents change much more rapidly as a function of θ. Additionally, we see that using ω_m close to the sensitivity peak in Fig. 2(a) yields converted currents in the amplitude of the ones excited in the fundamental harmonic. Figure 5(b) shows $S^0[\theta]$ and $S^1[\theta]$, depicting the strong increase (notice the different scales used) in the amplitude of S^1, versus the predicted more moderate increase in S^0 against the nonmodulated case (dashed). The purple line shows S for a $\omega_m/\omega = 0.432$, showing the dependence of the peak sensitivity angle on this parameter. In Fig. 5(c) we also present $\partial S/\partial \theta$ corresponding to (b), to illustrate the increased sensitivity.

D. Fast modulation

Another possible enhancement mechanism is revealed when examining higher modulation frequencies. While it might be challenging to achieve fast modulations (depending on the incident wave frequency and other system parameters), this physical mechanism exists and may be of use. When examining ΔS_1 for higher values of ω_m, we notice "ripples" that start occurring, when plotting $\Delta S_1(\omega_m/\omega)$, as seen in Fig. 6(a), in red. This effect happens because the dimer is no longer deep subwavelength at higher harmonics when the modulation is fast enough. Therefore, the interaction between the wires through the
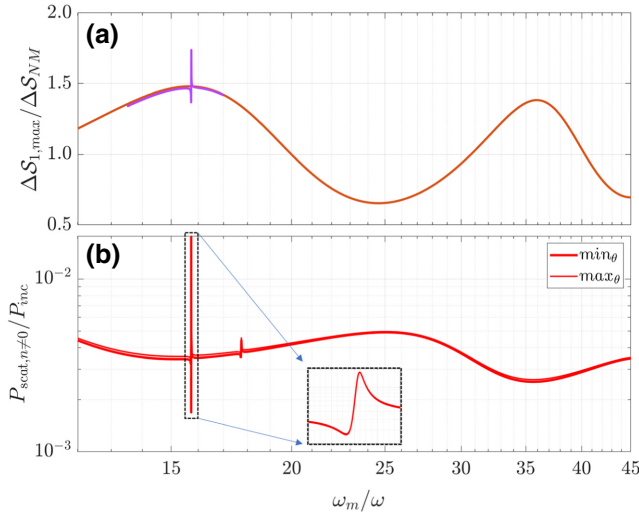
FIG. 6. Top: $S^1_{\max}$ as a function of ω_m/ω, with $10 < (\omega_m/\omega) < 45$. At $(\omega_m/\omega) > 20$, we see ripples in the sensitivity. Bottom: normalized energy as a function of ω_m/ω.

surrounding medium contributes a non-negligible phase difference, which causes the exciting field (incident + interaction) to couple better with the antisymmetric dimer mode, enhancing the sensitivity. Since this enhancement is nonresonant, it is milder than we saw previously. However, it can be incorporated with resonance by loading the wires with a resonant impedance in these frequencies, as shown in magenta in Fig. 6. The basic parameters are the same as in Sec. III A, and the additional resonant loading consists of $L_1 \approx 5.24$ nH, $C_1 \approx 0.195$ pF connected similarly to the results shown in Figs. 3(c) and 3(f). These are also demonstrated in the scattered power in Fig. 6(b). If we examine the enhancement around $\omega_m \approx 35\omega$ we see no peak in the scattered energy, indicating the nonresonant operation. However, around $\omega_m = 15.7\omega$, we see that the added resonance gives rise to a sharp peak in scattered power in the first harmonic, as it significantly increases the conversion efficiency.

E. Parametric amplification

So far, we show several ways the sensitivity benefits from incorporating time modulation. These are revolved around the careful design of the dimer resonances, combined with leveraging the frequency conversion processes that occur when applying periodic temporal modulation. In circuits, parametric amplifiers amplify the input voltage by modulating one of the reactive system elements. The most simple case, which we examine here, is the degenerate regime, where $\omega_m = 2\omega_0$ [28]. Recently, operating in this regime is also shown to enhance small antenna matching performance, and Q factor [14–16]. Since the gain in this regime depends on the phase between the incoming

signal and the modulation signal, we intuitively expect that this operation mode will both amplify the currents, and enhance the differences as a function of the DOA, due to differential gain. We start from Eqs. (5)–(7). We substitute $\omega_m = 2\omega_0$, and assume, in general, a phase difference of $\delta\phi$ between the modulation and incoming signals. The incident fields, as should be substituted into Eq. (5) are

$$[\tilde{E}_1] = [\ldots, 0, \tilde{E}_0^* e^{-j\delta\phi}, \tilde{E}_0 e^{j\delta\phi}, 0, \ldots]^T,$$
$$[\tilde{E}_2] = [\ldots, 0, \tilde{E}_0^* e^{-j\delta\phi + jkd\cos\theta}, \tilde{E}_0 e^{j\delta\phi - jkd\cos\theta}, 0, \ldots]^T.$$
(12)

The $\underline{\underline{\Gamma}}, \underline{\underline{G}}$ matrices would have the same structure as described in Eq. (5). Using these to solve the currents in the wires results in current components at all frequencies $\omega = (1 + 2n)\omega_0$. However, since the main interaction we are interested in is the parametric amplification that results from coupling $[-\omega_0, \omega_0]$, we tune the system parameters differently now. We have already established that working at the resonance frequency of the antisymmetric mode is preferable. In this case, it has two key effects: first, the baseline sensitivity of the unmodulated dimer will be around the best we can obtain without modulation. Second, the parametric amplification will increase the content of this antisymmetric mode. And lastly, operating near a system resonance will greatly simplify the analysis, rendering the currents for $\omega \neq \pm\omega_0$ negligible. Therefore, we use $C_0 \approx 27.2$ pF, and truncate $\underline{\underline{\Gamma}}$ and $\underline{\underline{G}}$ into 2×2 matrices, for the two main frequencies in the system $[-\omega_0, \omega_0]$. In addition, we increase the losses to see the effects of parametric amplification more clearly, adding a 2Ω resistance to the periodic loading.

$$\underline{\underline{\Gamma}}_{2\times2} = \begin{bmatrix} \gamma_0(-\omega_0) + \frac{1}{-j\omega_0 C_0 \Delta} & \frac{m}{j\omega_0 C_0 \Delta} \\ \frac{m^*}{-j\omega_0 C_0 \Delta} & \gamma_0(\omega_0) + \frac{1}{j\omega_0 C_0 \Delta} \end{bmatrix},$$
$$\underline{\underline{G}}_{2\times2} = \begin{bmatrix} G(d, -\omega_0) & 0 \\ 0 & G(d, \omega_0) \end{bmatrix}.$$
(13)

Yielding the wire currents

$$[\tilde{I}_2] = \left[\underline{\underline{\Gamma}}_{2\times2}\underline{\underline{G}}_{2\times2}^{-1}\underline{\underline{\Gamma}}_{2\times2} - \underline{\underline{G}}_{2\times2}\right]^{-1}([\tilde{E}_2]$$
$$+ \underline{\underline{\Gamma}}_{2\times2}\underline{\underline{G}}_{2\times2}^{-1}[\tilde{E}_1]),$$
$$[\tilde{I}_1] = \underline{\underline{\Gamma}}_{2\times2}^{-1}\left([\tilde{E}_1] + \underline{\underline{G}}_{2\times2}[\tilde{I}_2]\right).$$
(14)

In Fig. 7(a), the scattered power, normalized by the scattered power of the nonmodulated case, is presented as a function of the modulation depth m and of the DOA θ, for $\delta\phi = 0$. While there is a mild amplification overall, a very strong gain is obtained for a specific value $m \approx 0.11$. This operation regime strongly resembles the negative impedance parametric amplifier [28], so such a strong
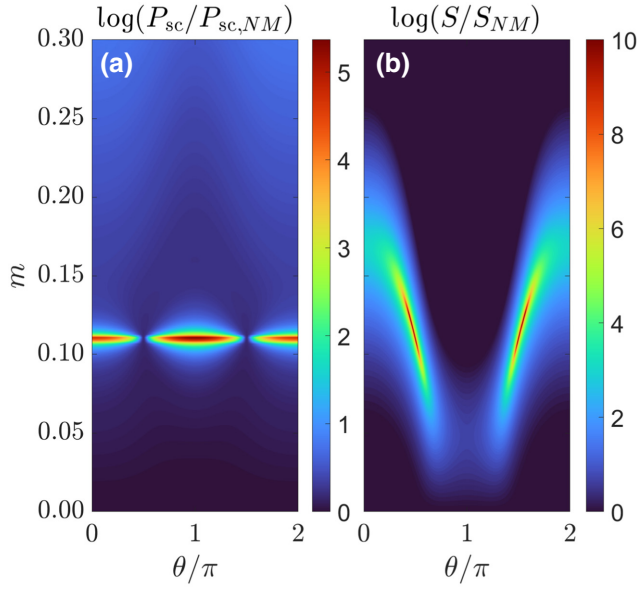
FIG. 7. (a) Total scattered power in the PA regime, normalized by the total scattered power of the nonmodulated case. Strong amplification occurs only around $m \approx 0.11$. (b) $S(\theta)$, normalized by the sensitivity of the nonmodulated case.

response around a specific m is expected. Working with this value of m comes along with a sensitive dependence on the choice of other system parameters. However, since the mere amplification of currents is not the sole purpose, we now examine the map of $\mathcal{S}$. In Fig. 7(b), The normalized sensitivity is presented as a function of m, θ. Here, we see that increased sensitivity can be obtained for a wide range of m values. Moreover, the modulation depth can be used to tune the angle around, which the optimal sensitivity is obtained, thus adding a great degree of flexibility that can be controlled by simple means. This shows that while the fundamental operation of the time-modulated system suggested here is similar to a parametric amplifier, the fact that other metrics play a key role is crucial, making this scheme relevant for a much broader range of parameters.

IV. CONCLUSIONS

In this work, we focus on studying the physical mechanisms that enhance a deeply subwavelength dimer's sensitivity to the DOA angle. We show that by carefully tuning the modulation parameters, different frequency-conversion processes contribute to increased sensitivity. Since the modulation parameters can be tuned, one obtains a highly flexible detector that can be tailored for wide-band operation and enhanced sensing in a specific, varying region of space. Modulating in a parametric amplification regime also contributes to a significant increase in sensitivity and exhibits tunability via the modulation depth and phase.

When designing a DOA detection system, the different effects can be combined. As an example, one can stack two

modulation tones, one to convert the incoming signal close to the desired antisymmetric resonance and one to enhance it parametrically.

Overall, we show that the richer physical interactions within the sensing system caused by the temporal modulation can be used to enhance DOA detection in various ways. This study can benefit many applications where the space occupied by the detection system must be extremely small, and many different branches can benefit from this research route.

ACKNOWLEDGMENT

APPENDIX A: INCIDENT AND SCATTERED POWER

Let us assume that for a specific frequency we have the currents I_1, I_2 in the dimer wires. The far fields generated by the dimer are [29]

$$
\begin{aligned}
\mathbf{E}_{\rm sc} &= -\frac{\eta k}{4}\sqrt{\frac{2}{\pi k\rho}}\Big[I_1 e^{-jk\rho - j\,(kd\cos(\varphi)/2) - j\,(\pi/4)} \\
&\quad + I_2 e^{-jk\rho + j\,(kd\cos(\varphi)/2) - j\,(\pi/4)}\Big]\hat{z} \\
&= -\frac{\eta k}{4}\sqrt{\frac{2}{\pi k\rho}}e^{-jk\rho - j\,(\pi/4)}\Big[I_1 e^{-j\,(kd\cos(\varphi)/2)} \\
&\quad + I_2 e^{j\,(kd\cos(\varphi)/2)}\Big]\hat{z}
\end{aligned}
\tag{A1}
$$

and the corresponding magnetic field is

$$
\mathbf{H}_{\rm sc} = \frac{1}{\eta}\hat{\rho}\times\mathbf{E}_{\rm sc} = \frac{1}{\eta}E_{\rm sc}\,\hat{\varphi}.
\tag{A2}
$$

This yields the scattered power per unit length

$$
\begin{aligned}
P_{\rm sc} &= \frac{1}{2}{\rm Re}\int_0^{2\pi}\mathbf{E}_{\rm sc}\times\mathbf{H}_{\rm sc}^*\rho d\varphi \\
&= \frac{\eta^2 k^2\rho}{16}\frac{2}{\pi k\rho}|e^{-jk\rho - j\,(\pi/4)}|^2\int_0^{2\pi}d\varphi \\
&\quad \Big|I_1 e^{-j\,(kd\cos(\varphi)/2)} + I_2 e^{j\,(kd\cos(\varphi)/2)}\Big|^2.
\end{aligned}
\tag{A3}
$$

Performing the integration, we get

$$
\begin{aligned}
P_{\rm sc} &= \frac{\eta^2 k^2\rho}{16}\frac{2}{\pi k\rho}|e^{-jk\rho - j\,(\pi/4)}|^2\int_0^{2\pi}d\varphi(|I_1|^2 + |I_2|^2) \\
&\quad + 2\Re\left\{|I1||I_2|e^{-jkd\cos(\varphi) - \angle(I_1, I_2)}\right\} \\
&= \frac{\eta^2 k}{4}\left([|I_1|^2 + |I_2|^2] + 2J_0(kd){\rm Re}\left\{I_1 I_2^*\right\}\right)
\end{aligned}
\tag{A4}
$$

Next, P_{inc} is composed of

$$P_{\text{inc}} = \frac{1}{2}\text{Re}\left\{E_{\text{wire}}^{\text{inc}}I_{\text{wire}}^{*}\right\} + \frac{1}{2}\text{Re}\left\{E_{\text{other wire}}^{\text{inc}}I_{\text{other wire}}^{*}\right\}.$$
(A5)

For each wire, the current can be expressed as

$$I_{\text{wire}} = \alpha E_{\text{wire}} = \alpha\left(E^{\text{inc}} + G(d)I_{\text{other wire}}\right)$$
(A6)

And since the problem is symmetric, we can use it for each wire. Hence,

$$P_{\text{inc}} = \frac{1}{2}\text{Re}\left\{\alpha^{*}(|E_1^{\text{inc}}|^2 + E_1^{\text{inc}}G^{*}(d)I_2^{*})\right\}$$
$$+ \frac{1}{2}\text{Re}\left\{\alpha^{*}(|E_2^{\text{inc}}|^2 + E_2^{\text{inc}}G^{*}(d)I_1^{*})\right\}.$$
(A7)

When modulation is present, we need, in general, to sum up all the contribution from all existing harmonics.

---

[1] N. Behdad, M. A. Al-Joumayly, and M. Li, Biologically inspired electrically small antenna arrays with enhanced directional sensitivity, IEEE Antennas Wirel. Propag. Lett. **10**, 361 (2011).

[2] S. Yi, M. Zhou, Z. Yu, P. Fan, N. Behdad, D. Lin, K. X. Wang, S. Fan, and M. Brongersma, Subwavelength angle-sensing photodetectors inspired by directional hearing in small animals, Nat. Nanotechnol. **13**, 1143 (2018).

[3] A. M. Elfrgani and R. G. Rojas, Biomimetic antenna array using non-Foster network to enhance directional sensitivity over broad frequency band, IEEE Trans. Antennas Propag. **64**, 4297 (2016).

[4] L. Goltcman and Y. Hadad, Scattering from Artificial Piezoelectriclike Meta-Atoms and Molecules, Phys. Rev. Lett. **120**, 054301 (2018).

[5] E. S. Cassedy and A. A. Oliner, Dispersion relations in time-space periodic media: Part I—Stable interactions, Proc. IEEE **51**, 1342 (1963).

[6] C. Kurth, Steady-state analysis of sinusoidal time-variant networks applied to equivalent circuits for transmission networks, IEEE Trans. Circuits Syst. **24**, 610 (1977).

[7] A. K. Kamal, A parametric device as a nonreciprocal element, Proc. IRE **48**, 1424 (1960).

[8] D. L. Sounas, C. Caloz, and A. Alu, Giant non-reciprocity at the subwavelength scale using angular momentum-biased metamaterials, Nat. Commun. **4**, 1 (2013).

[9] N. A. Estep, D. L. Sounas, J. Soric, and A. Alù, Magnetic-free non-reciprocity and isolation based on parametrically modulated coupled-resonator loops, Nat. Phys. **10**, 923 (2014).

[10] S. Qin, Q. Xu, and Y. E. Wang, Nonreciprocal components with distributedly modulated capacitors, IEEE Trans. Microw. Theory Tech. **62**, 2260 (2014).

[11] M. Mirmoosa, G. Ptitcyn, V. Asadchy, and S. Tretyakov, Time-Varying Reactive Elements for Extreme Accumulation of Electromagnetic Energy, Phys. Rev. Appl. **11**, 014024 (2019).

[12] Y. Hadad, D. L. Sounas, and A. Alu, Space-time gradient metasurfaces, Phys. Rev. B **92**, 100304 (2015).

[13] Y. Shi, S. Han, and S. Fan, Optical circulation and isolation based on indirect photonic transitions of guided resonance modes, ACS Photonics **4**, 1639 (2017).

[14] H. Li, A. Mekawy, and A. Alù, Beyond Chu's Limit with Floquet Impedance Matching, Phys. Rev. Lett. **123**, 164102 (2019).

[15] P. Loghmannia and M. Manteghi, Broadband parametric impedance matching for small antennas using the bode-Fano limit: Improving on Chu's limit for loaded small antennas, IEEE Antennas Propag. Mag. **64**, 55 (2022).

[16] A. Mekawy, H. Li, Y. Radi, and A. Alù, Parametric Enhancement of Radiation from Electrically Small Antennas, Phys. Rev. Appl. **15**, 054063 (2021).

[17] A. Shlivinski and Y. Hadad, Indirect time-modulation of antennas: A venue beyond size dependent bounds, ArXiv:2209.04841, 2022.

[18] C. Caloz and Z. Deck-Léger, Spacetime metamaterials—Part II: Theory and applications, IEEE Trans. Antennas Propag. **68**, 1583 (2020).

[19] A. Kord, D. L. Sounas, and A. Alù, Microwave nonreciprocity, Proc. IEEE **108**, 1728 (2020).

[20] V. Asadchy, A. Lamprianidis, G. Ptitcyn, M. Albooyeh Rituraj, T. Karamanos, R. Alaee, S. Tretyakov, C. Rockstuhl, and S. Fan, Parametric Mie Resonances and Directional Amplification in Time-Modulated Scatterers, Phys. Rev. Appl. **18**, 054065 (2022).

[21] A. Shlivinski and Y. Hadad, Beyond the Bode-Fano Bound: Wideband Impedance Matching for Short Pulses using Temporal Switching of Transmission-Line Parameters, Phys. Rev. Lett. **121**, 204301 (2018).

[22] O. Silbiger and Y. Hadad, Optimization-Free Filter and Matched-Filter Design Through Spatial and Temporal Soft Switching of the Dielectric Constant, Phys. Rev. Appl. **19**, 014047 (2023).

[23] E. Galiffi, S. Yin, and A. Alú, Tapered photonic switching, Nanophotonics **11**, 3575 (2022).

[24] C. He, X. Liang, Z. Li, J. Geng, and R. Jin, Direction finding by time-modulated array with harmonic characteristic analysis, IEEE Antennas Wirel. Propag. Lett. **14**, 642 (2015).

[25] X. Fang, M. Li, J. Han, D. Ramaccia, A. Toscano, F. Bilotti, and D. Ding, Accurate direction–of–arrival estimation method based on space–time modulated metasurface, IEEE Trans. Antennas Propag. **70**, 10951 (2022).

[26] Y. Hadad and D. Sounas, Space-time modulated loaded-wire metagratings for magnetless nonreciprocity and near-complete frequency conversion, ArXiv:1906.00215 2019.

[27] S. Tretyakov, *Analytical Modeling in Applied Electromagnetics* (Artech House, Boston & London, 2003).

[28] R. Collin, *Foundations for Microwave Engineering* (McGrew-Hill, New York, 1992).

[29] R. Harrington, Time-harmonic electromagnetic fields/ Harrington rf-New-York, Chichester, 2001.